Original Article

Mesoporous Magnetic Nanoparticles Functionalized With Quaternary Ammonium Salts as Targeted Nanocarriers for Doxorubicin Delivery in Breast Cancer Therapy

Sana Mousavi[1], Sedigheh Ehsanimehr[2], Tooba Mohammadi[1], Morteza Molaparast[3], Hajar Homa Maleki[4,5,*] and Vahid Shafiei-Irannejad[3,4,5,*]

[1]Student Research Committee, Urmia University of Medical Sciences, 57147-83734 Urmia, Iran
[2]Department of Organic Chemistry, Faculty of Chemistry, Urmia University, 57561-51818 Urmia, Iran
[3]Cellular and Molecular Research Center, Cellular and Molecular Medicine Research Institute, Urmia University of Medical Sciences, 57147-83734 Urmia, Iran
[4]Department of Chemistry, Institute of Inorganic and Materials Chemistry, University of Cologne, 50939 Cologne, Germany
[5]Center for Molecular Medicine Cologne, CMMC Research Center, 50931 Cologne, Germany

Abstract

Background: Nanotechnology offers promising strategies to overcome major limitations of conventional cancer chemotherapy, including poor targeting, systemic toxicity, and low drug bioavailability. This study focuses on developing a biocompatible magnetic nanocarrier modified with a quaternary ammonium salt to improve the delivery and therapeutic efficacy of doxorubicin in MDA-MB-231 breast cancer cells. **Methods:** Mesoporous silica-coated magnetic nanoparticles were modified with a Quaternary ammonium salt prepared from to enhance drug loading capacity, biocompatibility, stability, and anticancer efficacy. The nanocarrier was characterized using fourier-transform infrared spectroscopy (FTIR), scanning electron microscopy (SEM), dynamic light scattering (DLS), zeta potential, vibrating sample magnetometer (VSM), and X-ray diffraction (XRD) to evaluate its structure, size, and surface properties. *In vitro* drug release was evaluated at pH 7.4 and 5.5 to simulate physiological and tumor microenvironments, respectively. Biological performance and therapeutic potential were assessed through cellular uptake, cytotoxicity, apoptosis, and hemolysis assays. **Results:** The synthesized nanocarrier exhibited uniform size distribution, positive surface charge, and strong magnetic properties as confirmed by DLS, zeta potential, and VSM analyses. FTIR and XRD confirmed successful surface modification without compromising structural integrity. Drug release studies demonstrated pH-responsive behavior, with higher release under acidic conditions. Cellular uptake results exhibited efficient internalization of the nanocarriers by the cancer cells. The drug loaded nanocarrier induced significant cytotoxicity and apoptosis in cancer cells, while the hemolysis assay indicated good compatibility with red blood cells. **Conclusions:** The prepared quaternary ammonium salt-modified mesoporous magnetic nanocarrier demonstrates efficient physicochemical properties, biocompatibility, and enhanced anticancer activity. These findings suggest its potential as an effective and targeted drug delivery system for breast cancer chemotherapy.

Keywords: Doxorubicin, mesoporous silica, quaternary ammonium salt, cancer chemotherapy, breast cancer.

***Address for correspondence**: Hajar Homa Maleki, Department of Chemistry, Institute of Inorganic and Materials Chemistry, University of Cologne, 50939 Cologne, Germany; Center for Molecular Medicine Cologne, CMMC Research Center, 50931 Cologne, Germany. E-mail: h.maleki@uni-koeln.de; Vahid Shafiei-Irannejad, Cellular and Molecular Research Center, Cellular and Molecular Medicine Research Institute, Urmia University of Medical Sciences, 57147-83734 Urmia, Iran; Department of Chemistry, Institute of Inorganic and Materials Chemistry, University of Cologne, 50939 Cologne, Germany; Center for Molecular Medicine Cologne, CMMC Research Center, 50931 Cologne, Germany. E-mail: vshafiei@uni-koeln.de; vahid.shafiei@hotmail.com.

Introduction

Breast cancer is one of the most significant global health challenges, affecting millions of women worldwide [1]. Its onset is driven by a complex interaction of environmental, hormonal, and lifestyle factors [2]. Among its subtypes, triple-negative breast cancer (TNBC), represented by cell lines such as MDA-MB-231, is particularly aggressive and is characterized by the absence of estrogen, progesterone, and human epidermal growth factor receptor 2 (HER2) receptors, which limits the availability of targeted therapeutic options and results in poor clinical outcomes [3]. Consequently, systemic chemotherapy remains the cornerstone of treatment for metastatic breast cancer [4]. Doxorubicin (DOX) is a fundamental agent in chemotherapy regimens for various cancers, including breast cancer.

Its mechanism of action involves DNA intercalation, inhibition of topoisomerase II, and the generation of reactive oxygen species, ultimately leading to DNA damage and apoptosis [5]. However, despite its effectiveness, the clinical application of DOX is significantly limited by dose-dependent toxicity and non-specific distribution [6].

Due to its strong anticancer activity, DOX remains one of the most commonly used drugs in the treatment of metastatic breast cancer. However, its clinical use is often limited by serious side effects associated with systemic administration. These include anemia, hepatotoxicity, and most notably cardiotoxicity, which can significantly compromise patient safety and restrict the therapeutic dose [7,8]. Moreover, DOX-induced drug resistance in breast cancer cells is considered another cause of chemotherapy failure [9]. These limitations highlight the urgent need for advanced drug delivery systems that can improve therapeutic selectivity while minimizing toxicity [5].

In recent decades, nanotechnology has shown immense potential for targeted drug delivery, increasing the concentration of chemotherapy agents at tumor sites while diminishing their systemic side effects [10–13]. In this context, various nanoformulations of DOX have been designed to enhance its therapeutic effect and reduce toxicity [14,15]. For instance, Pegylated Liposomal DOX HCL (Doxil), approved in 1995, has been indicated to decrease tumor size and elevate survival rates of breast cancer patients when combined with agents such as 5-fluorouracil, paclitaxel, and cyclophosphamide [16]. More importantly, several nanocarrier systems have demonstrated promising results specifically in MDA-MB-231 breast cancer cells, showing improved cellular uptake, controlled and pH-responsive drug release, and increased cytotoxic and apoptotic effects. These findings underscore their potential for effectively targeting aggressive TNBC [17].

Mesoporous silica nanoparticles (MSNs) have attracted considerable attention in the biomedical field due to their unique structural properties. Their high porosity, large surface area, and modifiable particle size (ranging from 2 to 50 nm) enable efficient drug loading, controlled release, and enhanced cellular uptake. Furthermore, the surface of MSNs can be easily modified with polymers or targeting ligands, which helps improve their stability, biocompatibility, and ability to selectively accumulate in tumor tissues [18,19]. Several studies have shown that functionalizing MSNs with tumor-targeting ligands enables more precise delivery of therapeutic agents to cancer cells, ultimately enhancing treatment efficacy while reducing the side effects associated with conventional chemotherapy [20–22].

Moreover, magnetic nanoparticles (MNPs) have found great utility in diagnostic applications and therapeutic uses such as magnetic hyperthermia and targeted drug delivery [23]. MNPs can be guided to specific tissues in the body through the application of an external magnetic field, enhancing the accumulation of therapeutic agents in the cancerous areas while minimizing systemic exposure [24]. Furthermore, the utilization of biocompatible polymers like polyethyleneimine (PEI) aids drug internalization to the cells, making MNPs more efficient vehicles for drugs, including DOX [25].

On their own, porous substrates lack the capability to dependably store and discharge therapeutic agents under specific physiological conditions, such as those found in the tumor microenvironment. To overcome this limitation, polymeric networks and organic molecules are integrated to ensure regulated drug liberation and site-specific carrier targeting [26]. In this study, the aim was to modify the surface of magnetic mesoporous materials using a cationic polymer, PEI. Natural cationic polymers (NCPs) carry intrinsic positive charges, are derived from renewable sources, and can be considered biodegradable, nontoxic, and safe structures. By chemically modifying the available reactive sites on most NCPs, their physicochemical properties can be readily enhanced. These properties make NCP nanoparticles attractive candidates for various therapeutic applications, including drug delivery, gene therapy, and tissue engineering. PEI is a non-degradable polymer that contains primary, secondary, and tertiary amine groups, and it is widely recognized as one of the most commonly used cationic polymers across industries [27]. Notably, under physiological conditions, about 25% of these amine groups are protonated, endowing PEI with a high buffering capacity that can be advantageous in endosomal escape mechanisms [28]. Among the most important functional groups for surface modification of mesoporous materials are amino groups. Mesoporous materials bearing amino groups tend to agglomerate due to electrostatic interactions between positively charged amino groups and negatively charged surface hydroxyls, as well as hydrogen bonding [29].

One of the compounds used to modify these surfaces is quaternary ammonium salts based on PEI, which can be employed to enhance the delivery of the anticancer drug doxorubicin to tumor tissues while reducing its toxicity to other tissues. This approach increases drug loading, biocompatibility, stability, and efficacy against cancer cells. In this project, a high-efficiency polymeric nano-carrier is designed and synthesized for use in drug delivery systems. After designing and synthesizing a drug carrier based on silica-based magnetic mesopores modified with PEI, its physicochemical properties are characterized using techniques such as X-ray diffraction (XRD), zeta potential, fourier-transform infrared spectroscopy (FTIR), vibrating sample magnetometer (VSM), thermogravimetric analysis (TGA), dynamic light scattering (DLS), scanning electron microscopy (SEM), energy-dispersive X-ray spectroscopy (EDX), etc. In this study, we utilized Doxorubicin as a representative anticancer payload encapsulated within the developed nanovector. We first evaluated the vehicle's bio-

compatibility via a red blood cell hemolysis test before initiating biological experiments. To determine the formulation's impact on breast cancer, we treated cultured MDA-MB-231 cells with the drug-loaded matrix and calculated the half-maximal inhibitory concentration (IC_{50}) using an 3-(4,5-dimethylthiazol-2-yl)-2,5-diphenyl tetrazolium bromide (MTT) assay. We then analyzed apoptosis and nuclear changes using fluorescence imaging. Lastly, cellular uptake experiments were executed to track how efficiently the cells internalized the carrier.

Materials and Methods

Materials and Apparatus

The human breast adenocarcinoma cell line, MDA-MB-231, was sourced from the Pasteur Institute of Iran's Cell Bank. Culture essentials, including Roswell Park Memorial Institute 1640 (RPMI-1640) medium, trypsin, and fetal bovine serum (FBS; PAA Laboratories), were procured from Gibco™ (UK). Penicillin G, streptomycin, branched polyethyleneimine (bPEI, average Mw ~25 kDa, Merck), tetraethyl orthosilicate (TEOS), and polyethylene glycol 400 (PEG 400) were obtained from Merck. MTT, 3-chloropropyltrimethoxysilane (CPTMS), Pluronic F-127, toluene, methanol, ethanol, hydrochloric acid, and methyl iodide were purchased from Sigma-Aldrich. Ferric chloride and ferrous chloride salts were also obtained from Sigma-Aldrich and used as received. Doxorubicin hydrochloride, with a chromatographic purity of 98.5%, was supplied by Ebewe (Tehran, Iran). All experiments were performed using deionized water purified through a Milli-Q water filtration system.

Characterizations

FTIR spectra were acquired using a Fourier-transform infrared spectrophotometer (Nexus 670, Thermo Nicolet, USA). TGA was performed using a LENSES STAPT-1000 calorimeter (Germany), with the temperature increasing from room temperature to 800 °C at a rate of 10 °C/min. XRD patterns were recorded using an X'Pert Pro diffractometer (Netherlands) with Cu Kα radiation. Magnetic measurements of the MNPs were performed at room temperature on a VSM (Newcastle upon Tyne, UK). Morphological characterization was performed via SEM 3200 imaging, while elemental composition was mapped using Hitachi's S-4160 EDX system (Japan).

Synthesis

Synthesis of Fe_3O_4 Nanoparticles (MNPs)

The co-precipitation technique was utilized to fabricate the MNPs based on a previously reported protocol [25]. To eliminate dissolved oxygen, 100 mL of deionized water was initially subjected to mechanical stirring under a steady nitrogen purge for 15 min. Next, $FeCl_3 \cdot 6H_2O$ (5.838 g) and $FeCl_2 \cdot 4H_2O$ (2.147 g) were introduced into the deoxygenated water, followed by a 30-min sonication step. The solution was then heated to 75–80 °C in a water bath, after which 20 mL of an aqueous ammonia solution (25 wt%) was infused dropwise until a distinctive black precipitate emerged, verifying Fe_3O_4 formation. Stirring was maintained for another 30 min under inert conditions, and the mixture was subsequently cooled to ambient temperature. The synthesized Fe_3O_4 cores were isolated via magnetic separation using an external neodymium magnet, rinsed thoroughly with distilled water and ethanol to eliminate residual impurities, and finally dried at 80 °C for 24 h.

Synthesis of $Fe_3O_4@SiO_2$

Fabrication of the $Fe_3O_4@SiO_2$ core-shell nanostructures was performed using a sol–gel approach according to established literature [25]. Initially, 1.5 g of the pre-synthesized Fe_3O_4 MNPs was dispersed in 20 mL of deionized water within a 500 mL flask, followed by a 20-min ultrasonication step to break up aggregates. Next, 200 mL of isopropanol was introduced dropwise, and the suspension underwent an additional 30 min of sonication to guarantee a homogeneous matrix. To initiate silica shell growth under continuous magnetic stirring, specific quantities of PEG 400 (5.36 g), deionized water (20 mL), TEOS (2 mL) as the silicon precursor, and an aqueous ammonia solution (10 mL, 25 wt%) were sequentially introduced. The mixture was allowed to react under ambient conditions for 28 h to complete the condensation process. The resulting $Fe_3O_4@SiO_2$ composites were then isolated via an external permanent magnet, rinsed extensively with distilled water and ethanol to strip away residual precursors, and collected.

Synthesis of Mesoporous Magnetite Nanoparticles of $Fe_3O_4@SiO_2@$SBA-15 (MMNPs)

Fabrication of the mesoporous silica-coated magnetic nanoparticles ($Fe_3O_4@SiO_2@$SBA-15 MMNPs) was carried out by adapting a template-directed protocol established by Hartono *et al.* [30]. In a typical setup, 1.25 g of Pluronic F127 copolymer was dissolved in 45 mL of deionized water in a 100 mL reaction flask under steady stirring until a clear solution was achieved. Next, concentrated hydrochloric acid (2.5 mL, 37 wt%), the pre-formed $Fe_3O_4@SiO_2$ cores (1 g), and TEOS (1.1 mL) as the silica precursor were systematically added to the reaction vessel. Following a 24-h stirring period at ambient temperature, the mixture was moved to an oven and kept at 60 °C for another 24 h. The resulting MMNPs were isolated from the suspension using a strong external magnet without an intermediate washing step, and the collected material was dried completely in a vacuum oven at 100 °C for 24 h. To remove the Pluronic F127 template, the synthesized nanoparticles were calcined in a furnace at 550 °C under N_2 atmosphere for 6 h. The resulting template-free MMNPs were then collected and stored for further functionalization.

Synthesis of CPTMS-modified magnetic mesoporous nanoparticles (CMMNPs)

The surface of the MMNPs was functionalized by reacting CPTMS with the hydroxyl groups on their external surface. In a typical procedure, 1 g of MMNPs was dispersed in 40 mL of toluene and sonicated for approximately 30 minutes. Subsequently, 4.1 mL of CPTMS was added to the mixture, which was further sonicated for 20 minutes and then stirred at 50 °C for 24 hours.

After the reaction, the resulting CMMNPs were separated using an external magnet, thoroughly washed with methanol and acetone, and finally dried in a vacuum oven at 60 °C.

Functionalization of CMMNPs With PEI

The surface of the CMMNPs was further functionalized by reacting PEI with the surface hydroxyl groups. In this procedure, 1 g of unmodified CMMNPs was dispersed in 30 mL of distilled water and sonicated for 30 minutes. Subsequently, 1 g of PEI, dissolved in aqueous acetic acid, was added to the mixture and vigorously stirred at 25–30 °C for approximately 5 hours.

The resulting product was then collected using a permanent magnet and washed three times with deionized water and ethanol to remove any unreacted reagents. Finally, the purified precipitate was dried in a vacuum oven at 60 °C.

Preparation of Quaternary Ammonium Mesoporous Magnetic Nanoparticles (QA-MMNPs)

To synthesize QA-MMNPs, 0.27 g of amino-functionalized CMMNPs, 0.5 mL of methyl iodide (8.0 mmol), 0.38 g of sodium bicarbonate (4.0 mmol), and 15 mL of anhydrous methanol were combined in a 25 mL reaction flask and heated under reflux. The reaction was maintained at the boiling point of methanol with continuous magnetic stirring for approximately 72 hours. Additional methyl iodide (0.2 mL) was added after 24 and 48 hours to drive the quaternization reaction to completion.

After completion, the reaction mixture was cooled to room temperature, and the product was precipitated using cold diethyl ether. The precipitate was then washed several times with water to remove unreacted reagents and dried under vacuum.

Cell Culture and Biological Tests

Evaluation of Encapsulation Efficiency and Loading Capacity of Targeted MMNPs Nanocarrier

Briefly, 100 mg of the prepared MMNPs were dispersed in 5 mL of an aqueous DOX solution subjected to probe sonication for approximately 5 minutes to ensure a uniform and stable suspension, facilitating optimal drug-nanoparticle interaction. The resulting mixture of DOX and MMNPs was then continuously stirred for 24 hours under light-protected conditions to prevent photo-induced degradation of DOX and to allow sufficient time for effective drug adsorption onto and within the nanoparticle pores. Following incubation, the suspension was centrifuged at 8000 rpm for 10 minutes to separate the DOX-loaded nanoparticles (DMNs) from the unbound drug in the supernatant. The concentration of unencapsulated DOX in the supernatant was determined by measuring its absorbance at 480 nm using a ultraviolet–visible (UV–Vis) spectrophotometer.

The encapsulation efficiency (EE%) and loading capacity (LC%) of the nanoparticles were calculated using the following formulas:

$$\%EE = [(\text{mass of initially added drug} - \text{mass of free “unentrapped drug” in the supernatant})/\text{mass of initially added drug}] \times 100 \quad (1)$$

$$\%LC = [(\text{mass of initially added drug} - \text{mass of free “unentrapped drug” in the supernatant})/\text{mass of nanoparticles}] \times 100 \quad (2)$$

In Vitro Drug Release Study

To evaluate the release behavior of DOX from the nanoparticles, 5 mg of DOX-loaded MMNPs were dispersed in 2 mL of phosphate-buffered saline (PBS) at two different pH values (5.5 and 7.4), simulating tumor and physiological environments, respectively. Each sample was placed in a microtube and incubated in a shaker at 80 rpm. At predetermined time intervals (1, 3, 6, 9, 12, 24, 48, 72, and 96 hours), the samples were centrifuged at 8000 rpm for 10 minutes. Subsequently, 2 mL of the supernatant was collected and replaced with the same volume of fresh PBS.

The concentration of DOX released into the medium at each time point was determined using a UV-Vis spectrophotometer at 480 nm based on a standard calibration curve.

General Cell Culture Procedure

The MDA-MB-231 cell line was cultured in RPMI medium supplemented with 10% FBS and 1% penicillin-streptomycin, and incubated at 37 °C in a humidified atmosphere containing 5% CO_2. When the cells reached the logarithmic growth phase and approximately 70–80% confluence, they were washed twice with PBS to reduce the influence of vitronectin. The cells were then treated with trypsin-EDTA solution and incubated under the same conditions to facilitate detachment. After incubation, the detached cells were collected using a sterile pipette and centrifuged at 1500 rpm for 5 minutes to remove residual trypsin-EDTA. Finally, the cell pellet was resuspended in fresh RPMI medium and transferred to a new culture flask for subsequent experiments.

Cell Viability Assay

The MTT assay was employed to evaluate the cytotoxicity of free DOX, blank nanocarrier (NC), and DOX-loaded nanocarrier (DOX-NC) on the MDA-MB-231 cell line. In brief, cells were seeded into a 96-well tissue culture plate at a density of 1×10^4 cells per well and allowed to adhere for 24 hours under standard culture conditions. The following day, cells were treated with various concentrations of blank NC, free doxorubicin, and DOX-loaded NC for 48 hours according to the experimental protocol. After incubation, the culture medium was aspirated, and the cells were washed with PBS. Fresh medium containing 200 µL of MTT solution (2 mg/mL) was then added to each well, and the cells were incubated for an additional 4 hours. Subsequently, the medium was replaced with 200 µL of pure dimethyl sulfoxide (DMSO) to dissolve the intracellular formazan crystals, resulting in a violet-colored solution. Finally, the absorbance of the solution was measured at 570 nm using a microplate reader (DYNEX MRX, USA).

Cellular Uptake by Fluorescent Microscopy

To evaluate the cellular uptake of DOX-loaded nanocarrier, MDA-MB-231 cells (5×10^5 cells per well) were plated in 6-well plates containing RPMI medium and allowed to grow for 24 hours until they reached confluence. The cells were then exposed to IC_{50} concentrations of DOX-NC, blank NC, and free DOX for 1 and 3 hours. After treatment, the medium was carefully removed, and the cells were fixed using 4% paraformaldehyde for 15 minutes. The fixed cells were then rinsed three times with cold PBS (pH 7.4) to remove any residual reagent. Finally, cellular uptake was visualized and analyzed using a fluorescence microscope (Nikon Eclipse Ts2R, Japan).

In Vitro Hemolysis Assay

The biocompatibility of the targeted NC was evaluated using human red blood cells (HRBCs). Briefly, 2 mL of stabilized HRBC suspension was centrifuged at 3000 rpm for 10 minutes, after which the supernatant was carefully removed. The resulting cell pellet was washed several times with PBS to ensure purity. The purified HRBCs were then diluted tenfold with PBS and exposed to varying concentrations of targeted NC (20, 10, 5, 2.5, 1.2, 0.6, 0.3, and 0.1 µg/mL). All samples were gently agitated in a shaker incubator at 37°C for 4 hours. Following incubation, the samples were centrifuged at 13,000 rpm for 15 minutes, and the supernatants were collected. The optical density (OD) of hemoglobin released into the supernatant was measured using an enzyme-linked immunosorbent assay (ELISA) reader at 490 nm. The relative cell viability at each nanoparticle concentration was calculated using the following formula:

$$\text{Hemolysis rate} = \frac{OD_{sample} - OD_{PBS}}{OD_{water} - OD_{PBS}} \times 100 \quad (3)$$

Apoptosis Assay

4′,6-Diamidino-2-phenylindole (DAPI) nuclear staining was used to evaluate the apoptotic effects of the nanoparticles on MDA-MB-231 cells. In brief, exponentially growing cells (5×10^5 cells per well) were seeded into 6-well plates and incubated for 24 hours to allow attachment and growth. The cells were then treated with the IC_{50} concentration of DOX/MMNPs (1.2 μM) and incubated for 48 hours. After treatment, the cells were collected by centrifugation and washed twice with PBS. Fixation was carried out using 3.7% paraformaldehyde at 37 °C for 10 minutes, followed by permeabilization with 0.2% Triton X-100 (v/v) for 5 minutes. The cells were then stained with DAPI solution (100 nM) and incubated for 5 minutes in the dark at 37 °C. Finally, excess stain was removed by washing with PBS, and nuclear morphological changes associated with apoptosis were examined under a fluorescence microscope (Nikon Eclipse Ts2R, Japan).

Statistical Analysis

Data are presented as mean ± standard deviation (SD). Statistical analysis was performed using one-way analysis of variance (ANOVA) in GraphPad Prism 6 to evaluate differences among groups, as commonly applied in biomedical research. Statistical significance was defined as $p < 0.05$.

Results

Synthesis of QA-MMNPs

The specific quaternary magnetic nanocarrier was prepared as described. Initially, a sol-gel strategy was applied to encapsulate the synthesized MNPs within a silica shell using TEOS inside an isopropanol matrix to yield Fe_3O_4@SiO_2. Subsequently, an ordered mesoporous structure was fabricated over the silica surface via a template-directed sol-gel pathway assisted by Pluronic F127 copolymer surfactants. The outer surface of these MMNPs was then chemically activated through silanization, involving a covalent reaction between CPTMS and the exposed surface-bound hydroxyl moieties. Finally, PEI was grafted onto the CMMNPs nanoparticles to produce the quaternary ammonium magnetic nanocarrier, resulting in the QA-MMNPs (Scheme 1).

FTIR Analysis

The QA-MMNPs nanocarrier was analyzed using FTIR spectroscopy, and the spectra are shown in Fig. 1. In the Fe_3O_4@SiO_2 spectrum, the peak at 3420 cm^{-1} corresponds to the stretching vibrations of surface hydroxyl groups on the Fe_3O_4nanoparticles, while the peak at 573 cm^{-1} is attributed to the Fe–O bond vibration of Fe_3O_4.

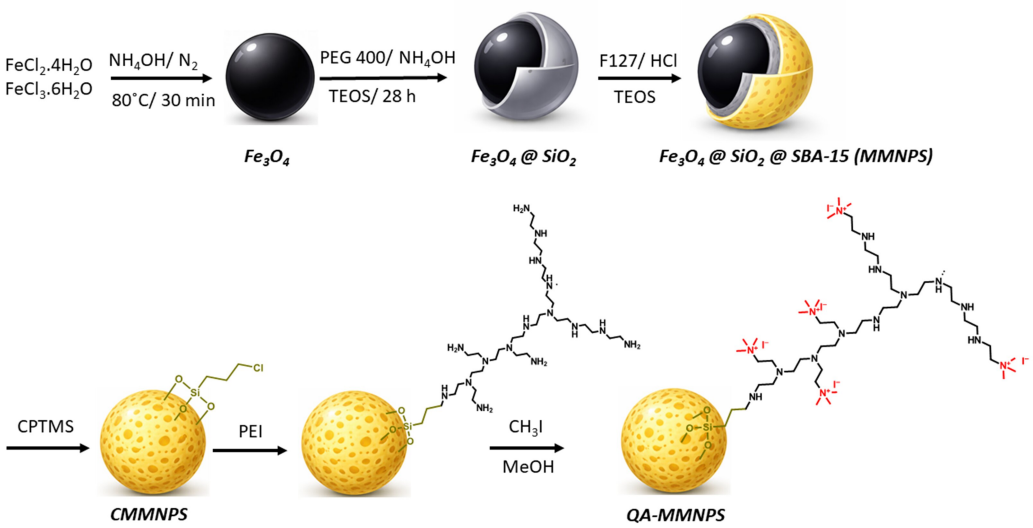

Scheme 1. Synthetic route for the preparation of the QA-MMNPs nanocarrier (drawn with ChemDraw software).

The successful grafting of SiO_2 onto the MNPs' surface is confirmed by distinctive peaks at 455 cm^{-1}, 786 cm^{-1}, 961 cm^{-1}, and 1075 cm^{-1}, representing Si–O–Si bending vibration, Si–O–Fe stretching vibration, and Si–O–Si symmetrical and asymmetric stretching vibrations, respectively. The FTIR spectrum of Fe_3O_4@SiO_2 @SBA-15 displays similar peaks to Fe_3O_4@SiO_2 but with increased intensity of hydroxyl group vibrations at 3389 cm^{-1} and 1628 cm^{-1}, corresponding to stretching and bending modes, due to the additional mesoporous SiO_2 shell. A weak band at 2926 cm^{-1} also appears, attributed to residual F-127 CH_2 groups. In the QA-MMNPs spectrum, the sharp peak at 1639 cm^{-1} corresponds to the quaternary ammonium salt, while bands at 1333 cm^{-1} and 1393 cm^{-1} are associated with C–N vibrations and bending vibrations of amine groups. Additionally, the band observed at 695 cm^{-1} corresponds to iodide ions, confirming the formation of the quaternary salt.

SEM and EDX Analysis

The surface morphology and particle size distribution of the synthesized quaternary magnetic nanocarrier were examined using SEM. Fig. 2**a** presents SEM images of both the untreated Fe_3O_4 (MNPs) and the targeted QA-MMNPs nanocarrier at two different magnifications. The SEM images of the untreated MNPs reveal significant agglomeration, attributed to Van der Waals forces between the particles. In contrast, the SEM images of the QA-MMNPs show reduced agglomeration and minimal clustering following surface modification of the MNPs. The nanoparticles are uniformly dispersed within the polymer matrix, indicating successful integration into the polymeric network. Additionally, an increase in particle size is observed, with the average diameter ranging from approximately 22 to 36 nm.

To further characterize the chemical composition of the synthesized QA-MMNPs, EDX analysis was performed alongside SEM. The elemental mapping of QA-MMNPs, shown in Fig. 2**b**, confirms the presence of carbon (C), oxygen (O), nitrogen (N), iron (Fe), and silicon (Si), verifying the stabilization and successful surface modification of the QA-MMNPs on the polymer substrate.

X-ray Diffraction

XRD analysis was conducted to investigate the crystal structures of both bare Fe_3O_4 nanoparticles and the QA-MMNPs nanocarrier. XRD is commonly employed to assess nanoparticle crystallinity and estimate average particle size. As shown in Fig. 3, the pure Fe_3O_4nanoparticles display characteristic diffraction peaks at 2θ values of 30.25°, 35.61°, 43.22°, 53.59°, 57.11°, and 62.70°, corresponding to the crystallographic planes (220), (311), (400), (331), (422), and (511), respectively. These peaks are in strong agreement with the standard magnetite pattern (JCPDS card no. 65-3107). The QA-MMNPs nanocarrier exhibits diffraction peaks at similar positions with comparable intensities, indicating that the Fe_3O_4crystalline structure remains intact during the synthesis process. However, observed shifts in peak positions between 10° and 30° 2θ are attributed to the presence of surface coatings such as PEI, SiO_2, and SBA-15, which alter the local crystal environment.

Thermogravimetric Analysis (TGA)

TGA of the QA-MMNPs nanocarrier is presented in Fig. 4, showing the weight loss as a function of temperature. The TGA curve reveals several distinct degradation stages. Initially, a minor weight loss between 50–160 °C corresponds to the evaporation of physically adsorbed water molecules. Following this, a significant weight loss occurs, indicating the decomposition of organic groups within the

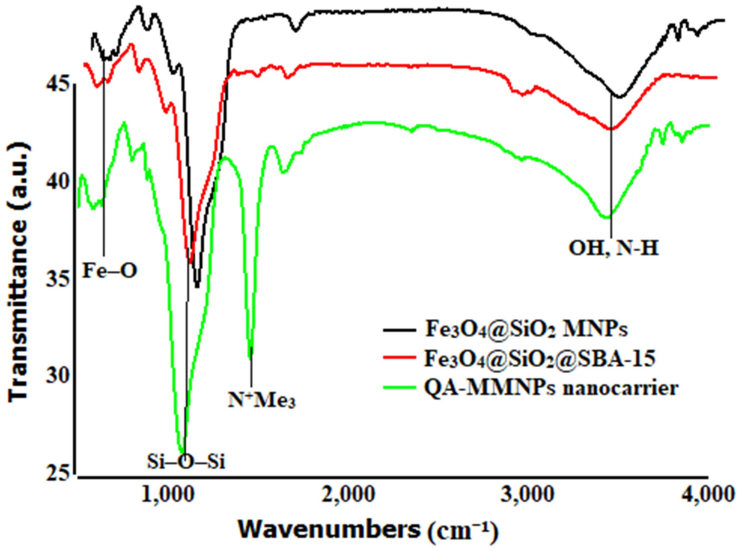

Fig. 1. FTIR spectra of Fe_3O_4@SiO_2 MNPs, Fe_3O_4@SiO_2@SBA-15 (MMNPs) and QA-MMNPs nanocarrier (drawn with qtiplot_0.9.8.3-3-Unofficial software).

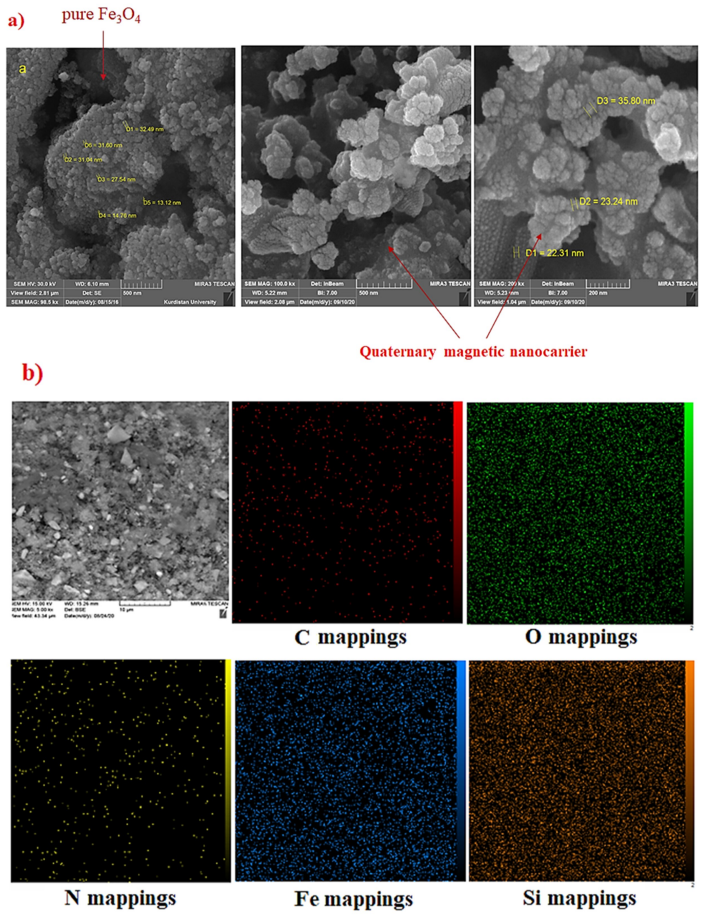

Fig. 2. a) SEM images of pure Fe_3O_4 and QA-MMNPs nanocarrier. b) Element mappings of the QA-MMNPs nanocarrier. Note: SEM images showcasing the structural evolution and shape definition of pure Fe_3O_4 compared to the QA-MMNPs. Elemental mappings of the QA-MMNPs nanocarrier, demonstrating the co-existence and uniform dispersion of constitutive elements across the scanned nanostructure area.

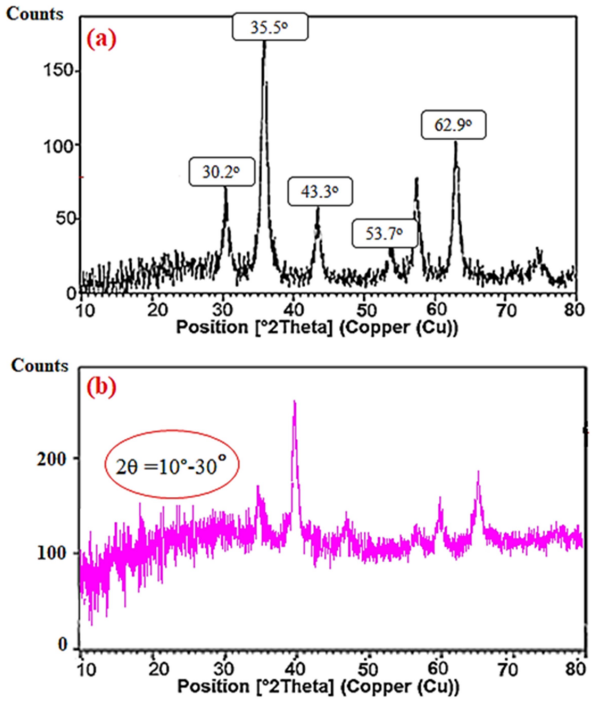

Fig. 3. XRD patterns of (a) pure Fe_3O_4 and (b) QA-MMNPs nanocarrier (drawn with qtiplot_0.9.8.3-3-Unofficial software).

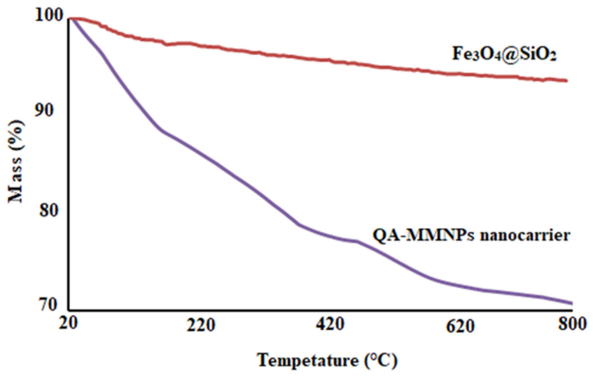

Fig. 4. TGA curves for Fe_3O_4@SiO_2 and QA-MMNPs nanocarrier (drawn with qtiplot_0.9.8.3-3-Unofficial software).

polymer matrix. In particular, the distinct thermal decline recorded within the 160–350 °C thermal window is closely tied to the pyrolytic destruction of the conjugated PEI polymeric fragments. The subsequent weight loss profile monitored between 350–470 °C represents the thermal cleavage of the underlying organosilane coupling network (CPTMS) anchoring the organic shell to the magnetic core. Weight loss between 470–650 °C is associated with the condensation and dehydration of the silica (SiO_2) layer. Finally, weight loss observed from 600–800 °C is linked to the overall decomposition of any residual organic components. The remaining char residue, approximately 67%, mainly comprises the magnetite core and the SiO_2 shell, confirming the successful surface functionalization of the QA-MMNPs nanocarrier with organic moieties.

VSM Measurement

Magnetic measurements of both the untreated MNPs and the QA-MMNPs nanocarrier were performed using a VSM within a magnetic field range of –8 to +8 kOe to evaluate their magnetic response. The hysteresis loops, shown in Fig. 5, indicate that the QA-MMNPs nanocarrier exhibits similar nonlinear, reversible, and negligible hysteresis behavior as the uncoated MNPs, confirming superparamagnetic properties characterized by zero coercivity and remanence. The saturation magnetization decreased from 66 emu/g for the pristine MNPs to 30 emu/g for the QA-MMNPs nanocarrier, which is attributed to the presence of the polymeric coating on the nanoparticle surface. This reduction confirms the successful surface modification of the nanoparticles.

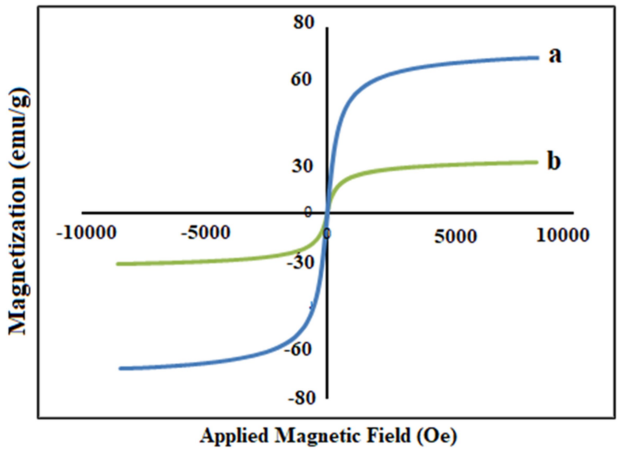

Fig. 5. VSM magnetization curves of a) uncoated MNPs b) QA-MMNPs nanocarrier (drawn with qtiplot_0.9.8.3-3-Unofficial software).

Table 1. Size, zeta potential, and polydispersity index of QA-MMNPs nanocarrier.

Blending nanoparticles	Average Size (nm)	PDI	Zeta potential (mV)
QA-MMNPs nanocarrier	326.3 ± 3.2	0.338	43.4 ± 2.7

Particle Size and Zeta Potential Analysis

Table 1 presents the results of the zeta potential analysis, particle size, alkylation percentage, and quaternization percentage of the QA-MMNPs nanocarrier. The zeta potential of the synthesized QA-MMNPs dispersed in deionized water was measured to be +43.4 ± 2.7 mV, indicating good colloidal stability due to the positively charged surface. DLS analysis was conducted using a Zetasizer instrument to determine both the particle size and zeta potential. The average hydrodynamic particle size was found to be approximately 326 nm, reflecting the overall size of the nanoparticles in suspension, including any polymeric coating and solvation layers.

Loading and In Vitro Drug Release Study

The DOX loading capacity is a crucial parameter for evaluating the efficiency of a drug delivery system. In this study, the EE% and LC% of the prepared QA-MMNPs nanocarrier were assessed, yielding an impressive EE% of approximately 99% and an LC% of about 9.9%. To further investigate the performance of the drug-loaded nanocarrier, an *in vitro* DOX release study was conducted to evaluate its stability and anticancer efficacy under different pH conditions. The release profiles were examined at pH 5.5 (acidic, mimicking the tumor microenvironment) and pH 7.4 (physiological pH) over various time intervals. As depicted in Fig. 6, the acidic environment significantly accelerated DOX release, which is attributed to the enhanced chemical interaction and weakened binding between DOX and the nanoparticle core under low pH conditions. The cumulative release percentages of DOX from the QA-MMNPs nanocarrier were 92.37% ± 3.27% at pH 5.5 and 46.53% ± 3.46% at pH 7.4, demonstrating effective pH-responsive drug release behavior.

In Vitro Cell Viability Assay

To evaluate cellular cytotoxicity, we conducted an MTT assay using varying dosages ranging from 0.125 to 4 µg/mL on three distinct groups: QA-MMNPs nanocarrier, DOX-QA-MMNPs nanocarrier, and free doxorubicin, in MDA-MB-231 cells over a 48-hour treatment period. As shown in Fig. 7, the blank nanocarrier (QA-MMNPs) maintained high cell viability (>75%) across all tested concentrations, indicating good biocompatibility of the final formulation. In contrast, both free DOX and DOX-QA-MMNPs exhibited dose-dependent cytotoxicity. Notably, DOX-QA-MMNPs demonstrated significantly greater cytotoxic effects compared to free DOX at equivalent concentrations, with cell viability decreasing to approximately 15% at 4 µg/mL. The IC_{50} values were calculated as 2103 ng/mL for free DOX and 797 ng/mL for DOX-QA-MMNPs, respectively.

In Vitro Cellular Uptake

Investigating the cellular uptake dynamics of both free DOX and DOX-QA-MMNPs nanocarrier in MDA-MB-231 cells provided evidence of intracellular drug/nanocarrier uptake, as illustrated in Fig. 8. Over an incubation period of 1 to 3 hours, fluorescence microscopy revealed the penetration of both free DOX and DOX-PEI-MMNPs into the cells. However, the fluorescence signal and the number of fluorescent cells

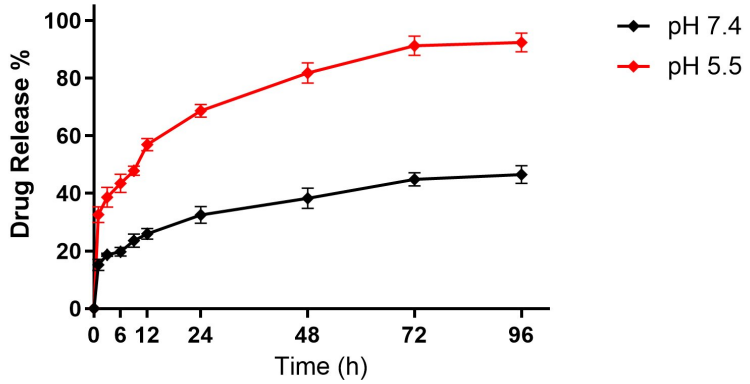

Fig. 6. *In vitro* release profiles of DOX from the targeted MMNPs nanocarrier under different pH conditions (pH 5.5 and pH 7.4) over a 96-hour period. The results showed that DOX was released more rapidly and in greater amounts under acidic conditions (pH 5.5), which mimics the tumor microenvironment, compared to physiological pH 7.4, indicating pH-responsive drug release behavior. The graph was plotted using GraphPad Prism 6 software.

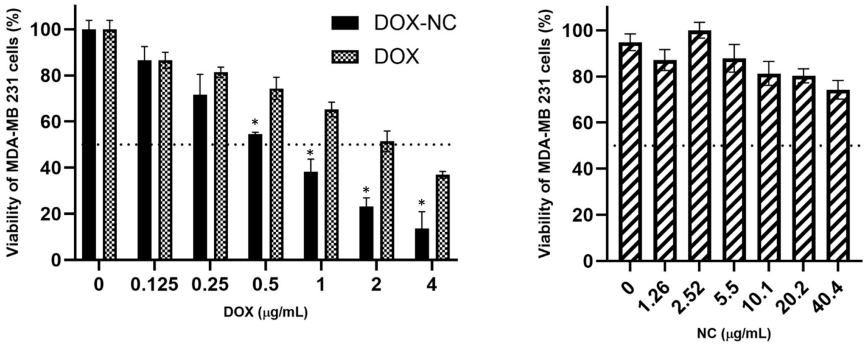

Fig. 7. MTT assay results illustrating the viability of MDA-MB-231 cells after 48 hours of treatment with varying concentrations (0.125 to 4 μg/mL) of NC, free DOX, and DOX-NC. Cell viability is expressed as a percentage relative to untreated controls. $*p < 0.05$. The NC alone showed high biocompatibility with minimal cytotoxic effects, maintaining cell viability around 80%. In contrast, both free DOX and DOX-NC exhibited dose-dependent cytotoxicity, with DOX-NC demonstrating enhanced efficacy in reducing cell viability compared to free DOX at equivalent concentrations. The graph was plotted using GraphPad Prism software.

Table 2. Quantitative comparison of QA-MMNPs nanocarrier with other reported polymeric nanocarriers.

Nanocarrier System	Encapsulation efficiency (EE%)	IC_{50} at 48 hours	pH–Responsive Release	Ref
QA-MMNPs nanocarrier	99%	0.797 μg/mL	92.37% $\pm$ 3.27% at pH 5.5 and 46.53% $\pm$ 3.46% at pH 7.4	-
PBCA Nanoparticles	49.3% $\pm$ 3.1%	0.0348 μg/mL	~49% at pH 7.4	[31]
PLGA Nanoparticles	~99%	greater than free doxorubicin	~50% at pH 7.4 and pH 5.5	[32]

appeared visually higher in the DOX QA-MMNPs group (Fig. 8, panels **c** and **d**) compared to the free DOX group (Fig. 8, panels **a** and **b**), suggesting possible interactions between the cellular layers and the designed nanocarrier. Furthermore, the investigation highlighted a visually observed time-dependent pattern in cellular uptake dynamics. Specifically, a noticeable increase in uptake was observed from 1 to 3 hours, with the 3-hour interval showing a higher apparent intracellular uptake than the initial hour of exposure.

Biocompatibility of the Targeted Nanoparticle

The hemolysis assay is a primary method for assessing the biocompatibility of drug-loaded nanocarriers at various concentrations in *in vivo* preclinical studies. Hemolysis is a crucial test to evaluate the potential erythrocyte-damaging

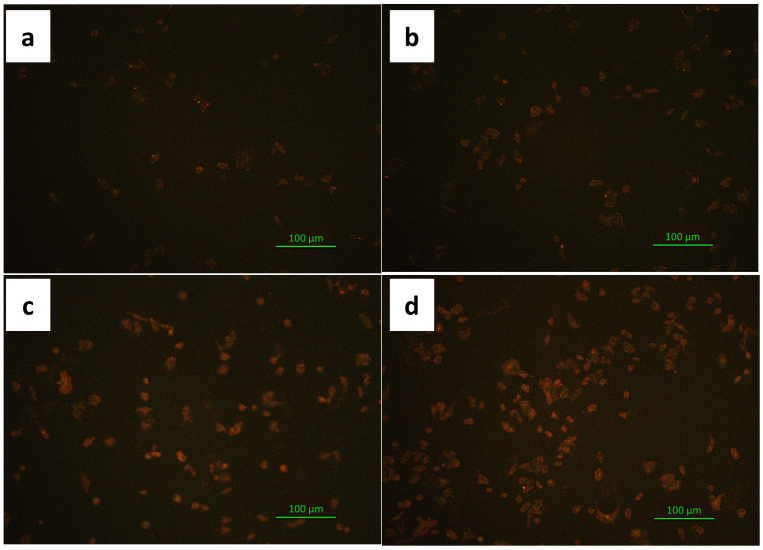

Fig. 8. Cellular uptake of free DOX (panels a and b) and DOX- QA-MMNPs nanocarrier (panels c and d) in MDA-MB-231 cells after 1 hour (panels a and c) and 3 hours (panels b and d) of incubation (Scale bar: 100 μm). Both formulations penetrated the cells, with DOX-QA-MMNPs nanocarrier demonstrating superior visual uptake efficacy. Uptake increased over time, especially at the 3-hour mark, indicating time-dependent dynamics in cellular internalization.

effects of NC. Evidence indicates that the hemolytic activity of nanocarriers depends on their physicochemical characteristics, particularly surface charge, functionalization, and the type of drug loaded. As shown in Fig. 9, erythrocyte hemolysis occurs through interaction with water. The hemolytic effects of the targeted QA-MMNPs nanocarriers on HRBCs were minimal, less than 5% hemolysis, across a range of concentrations under physiological conditions (pH 7.4, 37°C), remaining well within acceptable safety limits.

DAPI Staining

Chromatin density and morphology are key hallmarks of apoptosis, observable under a fluorescence microscope following DAPI staining. The chromatin morphological changes in MDA-MB-231 cells after treatment with DOX/QA-MMNPs nanocarrier were investigated. Representative fluorescence images are shown in Fig. 10. As observed, the nuclei of untreated control cells remained intact and homogenously stained with no significant morphological changes. Similar results were observed with cells treated with blank MMNPs. In contrast, cells exposed to free DOX and DOX-loaded QA-MMNPs showed clear signs of apoptosis, including chromatin condensation and nuclear fragmentation. Furthermore, the number of cells in treated groups was significantly decreased, indicating the cell growth inhibition potential of free DOX and DOX-loaded QA-MMNPs.

Discussion

This study successfully engineered a novel magnetic nanocarrier (QA-MMNPs) by functionalizing mesoporous silica-coated magnetite with quaternary ammonium salts and PEI. Structural analyses, including FTIR and XRD, confirmed that the surface modification was achieved without compromising the core's magnetic integrity, and such magnetic characteristics are crucial for enabling efficient magnetic separation of the QA-MMNPs nanocarrier from reaction mixtures using an external magnetic field. The resulting nanoparticles exhibited a uniform size distribution and a strong positive surface charge, which are essential for stable drug delivery and effective magnetic targeting within biological systems. The difference between SEM and DLS particle size measurements is actually to be expected, given the different physical principles behind the two measurements, and is further characterized by the surface chemistry of our particles. While SEM provides a direct visualization of the core size in the dry state, DLS measures the hydrodynamic diameter in a liquid medium. Our nanoparticles are coated with PEI. In the aqueous phase, the PEI chains are highly solvated and extended, creating a bulky hydration layer that moves with the particle and significantly increases its apparent hydrodynamic volume. However, during SEM sample preparation, this polymer shell is completely dehydrated and collapses. Furthermore, DLS is highly sensitive to even small amounts of particle clustering or aggregation in the colloidal state. Since the scattering intensity is proportional to d^6, the presence of a few larger clusters can significantly bias the average diameter towards the 300 nm range. In contrast, during SEM imaging, we naturally focus on individual, well-dispersed primary particles.

From a functional perspective, the system demonstrated an impressive drug encapsulation efficiency of

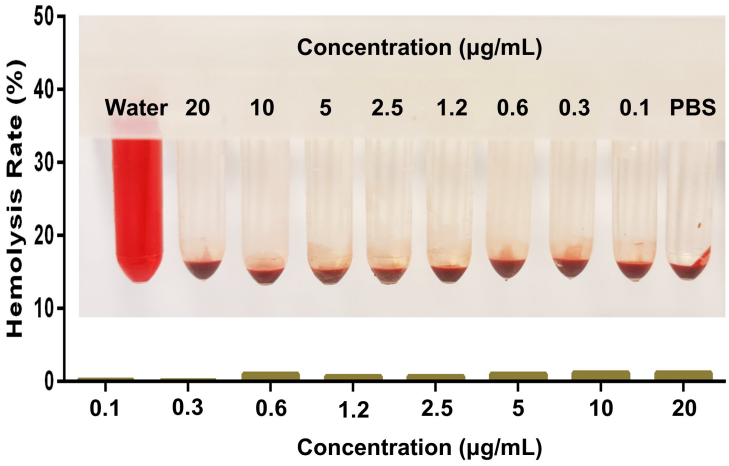

Fig. 9. Hemolysis rate of HRBCs after exposure to various concentrations (0.1–20 µg/mL) of MMNPs. Distilled water (positive control) caused complete hemolysis, while PBS (negative control) showed negligible hemolysis. The inset image visually supports the results by showing the absence of visible hemolysis in nanoparticle-treated samples compared to the bright red coloration in the positive control. The graph was plotted using GraphPad Prism 6 software.

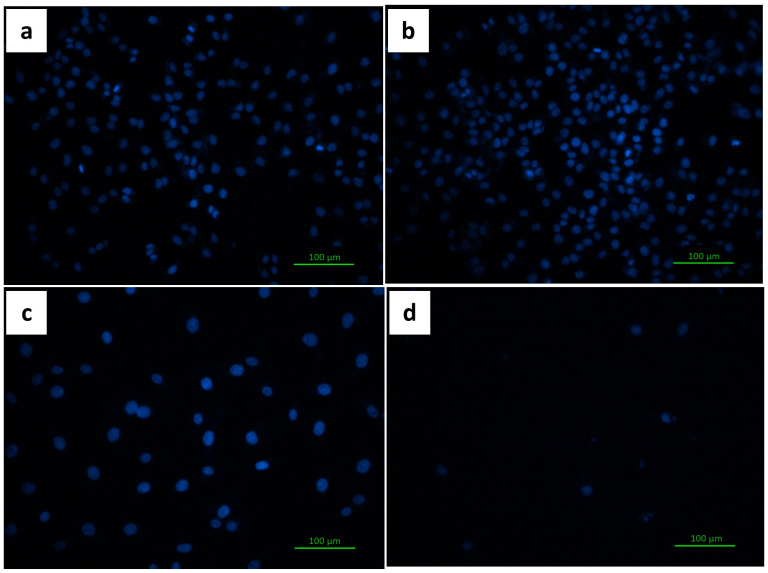

Fig. 10. Fluorescence microscopy images of MDA-MB-231 breast cancer cells stained with DAPI to visualize nuclear morphology after various treatments (Scale bar: 100 μm). (**a**) The untreated control group showed normal nuclear morphology and high cell density. (**b**) Cells treated with blank MMNPs showed no significant cytotoxic effect and intact nuclei. (**c**) Cells treated with free DOX exhibited moderate nuclear condensation, indicative of early apoptosis. (**d**) Cells treated with DOX-loaded QA-MMNPs, showed significant nuclear fragmentation and reduced cell density, suggesting enhanced apoptosis induction.

nearly 99%, attributed to the high specific surface area and regular pore network of the mesoporous core. A defining feature of this nanocarrier is its smart, pH-responsive release mechanism; it remains relatively stable at physiological pH but triggers a robust release of doxorubicin in the acidic microenvironment typical of tumor tissues. When tested against MDA-MB-231 breast cancer cells, the DOX-loaded nanocarrier showed significantly higher cellular uptake and cytotoxicity compared to the free drug, suggesting a marked improvement in therapeutic index. These results confirm that the enhanced anticancer activity is attributable to the DOX-loaded QA-MMNPs, while the QA-MMNPs alone exhibit minimal cytotoxicity, validating their suitability as a biocompatible drug delivery platform. Apoptotic assays further illustrated that treatment with DOX/MMNP nanocarriers caused significantly greater damage to nuclear and membrane integrity compared to untreated cells at an equivalent drug dosage.

In order to highlight the clinical potential and innovation of the developed QA-MMNPs, a comparison is made between this system and other known polymeric carriers for doxorubicin (DOX) delivery, such as poly(butylcyanoacrylate) (PBCA) and Poly(lactic-co-glycolic acid) (PLGA) nanoparticles [31,32]. As summarized in Table 2, QA-MMNPs show very high encapsulation efficiency (about 99%), attributed to the high specific surface area and regular pore network of the mesoporous core. In contrast, conventional polymers such as PBCA usually have lower loading due to the lack of defined internal porosity. Furthermore, our system exhibits pH-sensitive release kinetics. Structural changes and protonation at acidic pH (about 5.5) result in accelerated release, while alternative carriers rely on slower release mechanisms dependent on polymer degradation. This synergistic combination of high loading, pH responsiveness, and potent cytotoxicity demonstrates the distinct advantages of the QA-functionalized mesoporous framework over conventional dense polymer nanoparticles. Although the IC_{50} of our system is higher than the reported PBCA values, direct comparison should be made cautiously because the studies used different cell lines, exposure times, and nanocarrier chemistries.

Finally, the biocompatibility profiles indicated that these nanocarriers are remarkably safe, with hemolysis rates remaining well within the clinical safety threshold of 5%, confirming the systemic safety of the targeted MMNP nanocarriers for biological administration. Taken together, these findings position the QA-MMNP system as a highly efficient and selective platform for breast cancer chemotherapy, offering a strategic approach to maximize anti-tumor activity while mitigating the systemic toxicity often associated with conventional treatments.

Conclusions

Targeted drug delivery systems, especially nanoparticle-based platforms, show strong potential for improving cancer therapy. In this study, magnetic mesoporous nanoparticles were successfully synthesized and thoroughly characterized using various physicochemical techniques. The high encapsulation efficiency, coupled with a tumor-microenvironment-responsive release profile, underscores the system's capacity to selectively deliver doxorubicin where it is needed most. In cellular studies, the findings demonstrated that the synthesized nanocarrier system improved cellular permeability and cytotoxicity in MDA-MB-231 cells, contributing to enhanced therapeutic efficacy while reducing systemic side effects as evidenced by negligible toxicity toward red blood cells. Collectively, these results support QA-MMNPs as a promising, clinically relevant nanoplatform for breast cancer treatment, capable of enhancing therapeutic precision while limiting the off-target effects characteristic of conventional chemotherapy.

List of Abbreviations

ANOVA, Analysis of Variance; bPEI, Branched Polyethyleneimine; CMMNPs, CPTMS-modified Magnetic Mesoporous Nanoparticles; CPTMS, 3-Chloropropyltrimethoxysilane; DAPI, 4′,6-Diamidino-2-phenylindole; DLS, Dynamic Light Scattering; DMSO, Dimethyl Sulfoxide; DOX, Doxorubicin; EDX, Energy-Dispersive X-ray Spectroscopy; EE%, Encapsulation Efficiency; ELISA, Enzyme-Linked Immunosorbent Assay; FBS, Fetal Bovine Serum; FTIR, Fourier-Transform Infrared Spectroscopy; HER2, Human Epidermal Growth Factor Receptor 2; HRBCs, Human Red Blood Cells; IC_{50}, Half-Maximal Inhibitory Concentration; LC%, Loading Capacity; MMNPs, Mesoporous Magnetic Nanoparticles; MNPs, Magnetic Nanoparticles; MSNs, Mesoporous Silica Nanoparticles; MTT, 3-[4,5-Dimethylthiazol-2-yl]-2,5-diphenyltetrazolium Bromide; NCPs, Natural Cationic Polymers; PBCA, Poly(butylcyanoacrylate); PBS, Phosphate-Buffered Saline; PDI, Polydispersity Index; PEG 400, Polyethylene Glycol 400; PEI, Polyethyleneimine; PLGA, Poly(lactic-co-glycolic acid); QA-MMNPs, Quaternary Ammonium Mesoporous Magnetic Nanoparticles; RPMI-1640, Roswell Park Memorial Institute 1640; SD, Standard Deviation; SEM, Scanning Electron Microscopy; TEOS, Tetraethyl Orthosilicate; TGA, Thermogravimetric Analysis; TNBC, Triple-Negative Breast Cancer; UV-Vis, Ultraviolet–Visible; VSM, Vibrating Sample Magnetometer; XRD, X-ray Diffraction; NC, Nanocarrier; DOX-NC, DOX-loaded Nanocarrier; OD, Optical Density.

Availability of Data and Materials

The data supporting the findings of this study are available within the article. Additional data related to this study are available from the corresponding authors upon reasonable request.

Author Contributions

Conceptualization, S.M., S.E., M.M., T.M., H.H.M. and V.Sh.I.; Methodology, S.M., S.E., M.M., T.M., H.H.M. and V.Sh.I.; Investigation, S.M., S.E., M.M., and T.M., Writing-original Draft Preparation, S.M., S.E., M.M., and T.M.; Writing- Review and Editing, V.Sh.I. and H.H.M.; Supervision, V.Sh.I. and H.H.M.; Project administration, V.Sh.I. All authors read and approved the final manuscript. All authors agree to be accountable for all aspects of the work in ensuring that questions related to the accuracy or integrity of any part of the work are appropriately investigated and resolved.

Ethics Approval and Consent to Participate

Not applicable.

Acknowledgments

Not applicable.

Funding

This research received no external funding.

Conflict of Interest

The authors declare that they have no conflict of interests regarding the publication of this article, financial and/or otherwise.

References

[1] Łukasiewicz S, Czeczelewski M, Forma A, Baj J, Sitarz R, Stanisławek A. Breast Cancer—Epidemiology, Risk Factors, Classification, Prognostic Markers, and Current Treatment Strategies—An Updated Review. Cancers. 2021; 13: 4287. https://doi.org/10.3390/cancers13174287.

[2] Seiler A, Chen MA, Brown RL, Fagundes CP. Obesity, Dietary Factors, Nutrition, and Breast Cancer Risk. Current Breast Cancer Reports. 2018; 10: 14–27. https://doi.org/10.1007/s12609-018-0264-0.

[3] Bianchini G, Balko JM, Mayer IA, Sanders ME, Gianni L. Triple-negative breast cancer: challenges and opportunities of a heterogeneous disease. Nature reviews. Clinical oncology. 2016; 13: 674–690. https://doi.org/10.1038/nrclinonc.2016.66.

[4] Liedtke C, Kolberg HC. Systemic therapy of advanced/metastatic breast cancer-current evidence and future concepts. Breast care (Basel, Switzerland). 2016; 11: 275–281. https://doi.org/10.1159/000447549.

[5] Bisht A, Avinash D, Sahu KK, Patel P, Das Gupta G, Kurmi BD. A comprehensive review on doxorubicin: mechanisms, toxicity, clinical trials, combination therapies and nanoformulations in breast cancer. Drug Delivery and Translational Research. 2025; 15: 102–133. https://doi.org/10.1007/s13346-024-01648-0.

[6] Rawat PS, Jaiswal A, Khurana A, Bhatti JS, Navik U. Doxorubicin-induced cardiotoxicity: An update on the molecular mechanism and novel therapeutic strategies for effective management. Biomedicine & Pharmacotherapy. 2021; 139: 111708. https://doi.org/10.1016/j.biopha.2021.111708.

[7] Kuok CT, Lee HW, Huang CY, Cheng YC, Lin SC, Guo JW. Doxorubicin-Induced Cardiotoxicity in Breast Cancer: Mechanistic Pathways, Pharmacogenomic Modifiers, and Translational Strategies. Cardiovascular Toxicology. 2026; 26: 59. https://doi.org/10.1007/s12012-026-10132-9.

[8] Qiu Y, Jiang P, Huang Y. Anthracycline-induced cardiotoxicity: mechanisms, monitoring, and prevention. Frontiers in Cardiovascular Medicine. 2023; 10: 1242596. https://doi.org/10.3389/fcvm.2023.1242596.

[9] Luo F, Zhao J, Liu S, Xue Y, Tang D, Yang J, *et al*. Ursolic acid augments the chemosensitivity of drug-resistant breast cancer cells to doxorubicin by AMPK-mediated mitochondrial dysfunction. Biochemical Pharmacology. 2022; 205: 115278. https://doi.org/10.1016/j.bcp.2022.115278.

[10] Shafiei-Irannejad V, Rahimi M, Zarei M, Dinparast-Isaleh R, Bahrambeigi S, Alihemmati A, *et al*. Polyelectrolyte Carboxymethyl Cellulose for Enhanced Delivery of Doxorubicin in MCF7 Breast Cancer Cells: Toxicological Evaluations in Mice Model. Pharmaceutical Research. 2019; 36: 68. https://doi.org/10.1007/s11095-019-2598-3.

[11] Nguyen LNM, Ngo W, Lin ZP, Sindhwani S, MacMillan P, Mladjenovic SM, *et al*. The mechanisms of nanoparticle delivery to solid tumours. Nature Reviews Bioengineering. 2024; 2: 201–213. https://doi.org/10.1038/s44222-024-00154-9.

[12] Yan J, Zhao Z, Yu H, Sun F, Wang L, Du L, *et al*. Regulating lactate metabolism and remodeling the tumor microenvironment via a bio-hybrid nanoplatform for enhanced tumor photo-immunotherapy. Chemical Engineering Journal. 2026; 535: 175459. https://doi.org/10.1016/j.cej.2026.175459.

[13] Zhao Z, Sun F, Wang W, Li B, Liang Y, Wei D, *et al*. Nucleic acid-based nanogels with “offensive and defensive” effects for enhanced chemo-immunotherapy. Journal of controlled release: official journal of the Controlled Release Society. 2025; 385: 113977. https://doi.org/10.1016/j.jconrel.2025.113977.

[14] Chang YS, Sabu A, Kandel M, Lo CL, Roy E, Ramesan L, *et al*. Hydroxyapatite and doxorubicin-laden nanotherapeutics for effective multimodality cancer treatment boosted via mitochondrial calcium overload. Journal of controlled release: official journal of the Controlled Release Society. 2025; 388: 114368. https://doi.org/10.1016/j.jconrel.2025.114368.

[15] Molaparast M, Malekinejad H, Rahimi M, Shafiei-Irannejad V. Biocompatible functionalized graphene nanosheet for delivery of doxorubicin to breast cancer cells. Journal of Drug Delivery Science and Technology. 2022; 70: 103234. https://doi.org/10.1016/j.jddst.2022.103234.

[16] Rau KM, Lin YC, Chen YY, Chen JS, Lee KD, Wang CH, *et al*. Pegylated liposomal doxorubicin (Lipo-Dox®) combined with cyclophosphamide and 5-fluorouracil is effective and safe as salvage chemotherapy in taxane-treated metastatic breast cancer: an open-label, multi-center, non-comparative phase II study. BMC Cancer. 2015; 15: 423. https://doi.org/10.1186/s12885-015-1433-4.

[17] Badparvar F, Marjani AP, Salehi R, Ramezani F. pH/redox responsive size-switchable intelligent nanovehicle for tumor microenvironment targeted DOX release. Scientific Reports. 2023; 13: 22475. https://doi.org/10.1038/s41598-023-49446-x.

[18] Niculescu VC. Mesoporous Silica Nanoparticles for Bio-Applications. Frontiers in Materials. 2020; 7: 36. https://doi.org/10.3389/fmats.2020.00036.

[19] Huq TB, Anil Kumar Jeeja P, Dam SK, Das SS, Vivero-Escoto JL. Recent applications of mesoporous silica nanoparticles in gene therapy. Advanced Healthcare Materials. 2025; 14: 2404781. https://doi.org/10.1002/adhm.202404781.

[20] Gao Y, Gao D, Shen J, Wang Q. A Review of Mesoporous Silica Nanoparticle Delivery Systems in Chemo-Based Combination Cancer Therapies. Frontiers in chemistry. 2020; 8: 598722. https://doi.org/10.3389/fchem.2020.598722.

[21] Rahikkala A, Pereira SAP, Figueiredo P, Passos MLC, Araújo ARTS, Saraiva MLMFS, *et al*. Mesoporous Silica Nanoparticles for Targeted and Stimuli-Responsive Delivery of Chemotherapeutics: A Review. Advanced Biosystems. 2018; 2: 1800020. https://doi.org/10.1002/adbi.201800020.

[22] Gisbert-Garzarán M, Vallet-Regí M. Redox-responsive mesoporous silica nanoparticles for cancer treatment: Recent updates. Nanomaterials (Basel, Switzerland). 2021; 11: 2222. https://doi.org/10.3390/nano11092222.

[23] Alromi DA, Madani SY, Seifalian A. Emerging Application of Magnetic Nanoparticles for Diagnosis and Treatment of Cancer. Polymers. 2021; 13: 4146. https://doi.org/10.3390/polym13234146.

[24] Coene A, Leliaert J. Magnetic nanoparticles in theranostic applications. Journal of Applied Physics. 2022; 131: 160902. https://doi.org/10.1063/5.0085202.

[25] Ehsanimehr S, Moghadam PN, Dehaen W, Shafiei-Irannejad V. PEI grafted Fe_3O_4@ SiO2@ SBA-15 labeled FA as a pH-sensitive mesoporous magnetic and biocompatible nanocarrier for targeted delivery of doxorubicin to MCF-7 cell line. Colloids and Surfaces A: Physicochemical and Engineering Aspects. 2021; 615: 126302. https://doi.org/10.1016/j.colsurfa.2021.126302.

[26] Dutta Gupta Y, Mackeyev Y, Krishnan S, Bhandary S. Mesoporous silica nanotechnology: promising advances in augmenting cancer theranostics. Cancer Nanotechnology. 2024; 15: 9. https://doi.org/10.1186/s12645-024-00250-w.

[27] Zhao C, Zhou B. Polyethyleneimine-based drug delivery systems for cancer theranostics. Journal of Functional Biomaterials. 2022; 14: 12. https://doi.org/10.3390/jfb14010012.

[28] Jones GD, Langsjoen A, NEUMANN SMMC, Zomlefer J. The polymerization of ethylenimine. The Journal of Organic Chemistry. 1944; 9: 125–147. https://doi.org/10.1021/jo01184a002.

[29] Yang B, Picchetti P, Wang Y, Wang W, Seeger C, Bozov K, *et al*. Patterned immobilization of polyoxometalate-loaded mesoporous sil-

ica particles via amine-ene Michael additions on alkene functionalized surfaces. Scientific Reports. 2024; 14: 1249. https://doi.org/10.1038/s41598-023-50846-2.

[30] Hartono SB, Phuoc NT, Yu M, Jia Z, Monteiro MJ, Qiao S, *et al*. Functionalized large pore mesoporous silica nanoparticles for gene delivery featuring controlled release and co-delivery. Journal of Materials Chemistry B. 2014; 2: 718–726. https://doi.org/10.1039/C3TB21015D.

[31] Cabeza L, Ortiz R, Arias JL, Prados J, Ruiz Martinez MA, Entrena JM, *et al*. Enhanced antitumor activity of doxorubicin in breast cancer through the use of poly (butylcyanoacrylate) nanoparticles. International Journal of Nanomedicine. 2015; 10: 1291–1306. https://doi.org/10.2147/IJN.S74378.

[32] Yoo HS, Park TG. Biodegradable polymeric micelles composed of doxorubicin conjugated PLGA–PEG block copolymer. Journal of controlled release: official journal of the Controlled Release Society. 2001; 70: 63–70. https://doi.org/10.1016/S0168-3659(00)00340-0.

Editor's note: The Scientific Editors responsible for this paper were Xiaoyuan Ji and Kelong Fan.

Received: 1st April 2026; **Accepted**: 7th July 2026; **Published**: 31st July 2026